Lattice-matched *in-situ* construction of 2D/2D T-SrTiO$_3$/CsPbBr$_3$ heterostructure for efficient photocatalysis of CO$_2$ reduction

Su-Xian Yuan, Ke Su, You-Xiang Feng, Min Zhang*, Tong-Bu Lu

MOE International Joint Laboratory of Materials Microstructure, Institute for New Energy Materials and Low Carbon Technologies, School of Materials Science and Engineering, Tianjin University of Technology, Tianjin 300384, China

A R T I C L E   I N F O

A B S T R A C T

The elaborate regulation of heterostructure interface to accelerate the interfacial charge separation is one of practicable approaches to improve the photocatalytic CO$_2$ reduction performance of halide perovskite (HP) materials. Herein, we report an *in-situ* growth strategy for the construction of 2D CsPbBr$_3$ based heterostructure with perovskite oxide (SrTiO$_3$) nanosheet as substrate (CsPbBr$_3$/SrTiO$_3$). Lattice matching and matchable energy band structures between CsPbBr$_3$ and SrTiO$_3$ endow CsPbBr$_3$/SrTiO$_3$ heterostructure with an efficient interfacial charge separation. Moreover, the interfacial charge transfer rate can be further accelerated by etching SrTiO$_3$ with NH$_4$F to form flat surface capped with Ti−O bonds. The resultant 2D/2D T-SrTiO$_3$/CsPbBr$_3$ heterostructure exhibits an impressive photocatalytic activity for CO$_2$ conversion with a CO yield of 120.2 ± 4.9 μmol g^{-1} h^{-1} at the light intensity of 100 mW/cm^2 and water as electron source, which is about 10 and 7 times higher than those of the pristine SrTiO$_3$ and CsPbBr$_3$ nanosheets, surpassing the reported halide perovskite-based photocatalysts under the same conditions.

© 2023 Published by Elsevier B.V. on behalf of Chinese Chemical Society and Institute of Materia Medica, Chinese Academy of Medical Sciences.

Artificial photosynthesis can directly utilize inexhaustible solar energy to reduce CO$_2$ into high value-added fuels or chemicals, which can not only provide partial sustainable energy supply, but also effectively alleviate global climate change induced by the excessive emission of greenhouse gas [1–6]. In an ideal artificial photosynthesis system, water is a desirable electron source for CO$_2$ photoreduction, which furnishes a "green chemistry" route to generate value-added chemicals without employing any expensive sacrificial reagents [7]. That is, the redox capacities of photocatalysts should straddles the requirements of both the CO$_2$ reduction and H$_2$O oxidation potentials [8]. Based on this prerequisite, a variety of semiconductor materials with wide bandgap have been widely exploited as candidates for photocatalytic CO$_2$ reduction coupled with H$_2$O oxidation, such as metal oxides and sulfides [9–11], metal-organic frameworks [12], layered double hydroxides [13], conjugated polymers [14] and so on, but the photocatalytic performance is limited by the weak visible light response and severe charge recombination [15]. Up to now, most of the researches are focused on the amelioration of light-harvesting capacity and photogenerated carrier separation efficiency [16–18].

Among various semiconductor materials, halide perovskite (HP) nanocrystals (NCs) have been widely employed as promising can-

didate catalysts in the field of photocatalysis [19–22], owing to their fascinating photophysical properties such as robust light-harvesting ability and high separation efficiency of photogenerated carrier [23]. The CO$_2$ photoreduction activity of HP NC based catalysts have been notably meliorated through multifarious strategies such as morphology modification [24,25], decorating reduction [26–29] or oxidation cocatalysts [30–36]. However, the activity of current halide perovskite based catalysts for artificial is still low owing the deficient active site and/or insufficient separation of photogenerated carriers. Therefore, it is highly imperative to establish viable strategies to improve the performance of HP materials to meet the prerepuisite of practical applications. Recenlty, we have demonstrated that ultra-thin two-dimensional (2D) HP nanosheet (NS) exhibits higher catalytic activity for CO$_2$ photoreduction than conventional HP NCs, due to the increased low coordination metal atom ratio and short carrier diffusion distance of ultra-thin 2D HP NS [24]. In addition, it is widely recognized that the 2D materials are conducive to effective contact and charge separation between components in heterostructure [37,38]. Based on these analyses, herein we reported a simple lattice-matched *in-situ* growth strategy for the construction of 2D CsPbBr$_3$ based heterostructure with perovskite oxide (SrTiO$_3$) as substrate to improve the photocatalytic CO$_2$ reduction performance of HP materials. SrTiO$_3$ (space group $Pm\bar{3}m$) possess the same crystal structure with cubic CsPbBr$_3$, and its lattice constant is exactly 2/3 of

---

* Corresponding author.
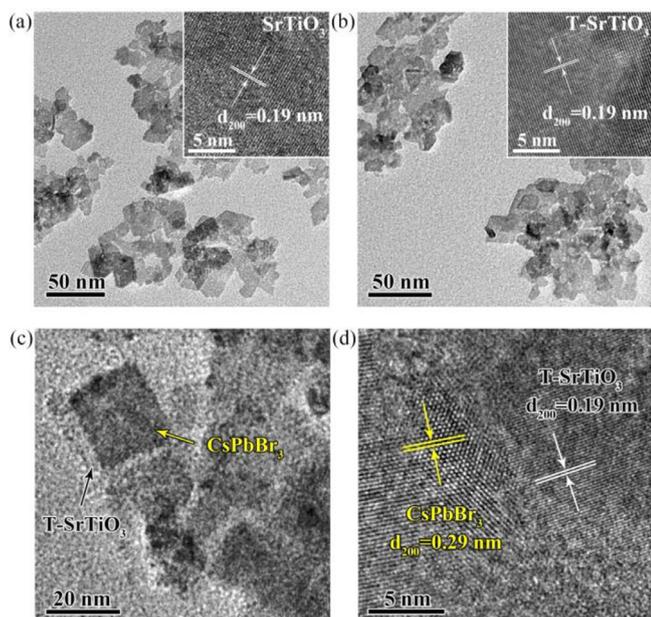 *E-mail address:* zm2016@email.tjut.edu.cn (M. Zhang).

Fig. 1. TEM images of (a) SrTiO₃ and (b) T-SrTiO₃. Insets are the corresponding HRTEM images. (c) TEM and (d) HRTEM images of T-SrTiO₃/CsPbBr₃.
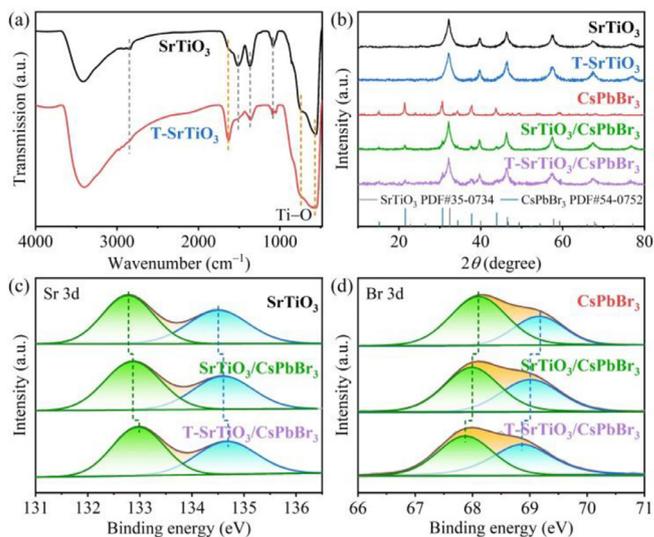

Fig. 2. (a) FTIR spectra of SrTiO₃ and T-SrTiO₃. (b) Powder XRD patterns of SrTiO₃, T-SrTiO₃, CsPbBr₃, SrTiO₃/CsPbBr₃ and T-SrTiO₃/CsPbBr₃. High-resolution XPS spectra of (c) Sr 3d and (d) Br 3d in SrTiO₃, SrTiO₃/CsPbBr₃ and T-SrTiO₃/CsPbBr₃.

$CsPbBr_3$ ($a = 3.905$ *vs.* 5.830 Å). Therefore, the two cells of $CsPbBr_3$ happen to match the three cells of $SrTiO_3$ in a disproportionate manner, and the lattice mismatch factor is only 0.47% [39]. This low mismatch provides a reasonable condition for $CsPbBr_3$ to *in-situ* grown tightly on the $SrTiO_3$ surface. Furthermore, considering that $SrTiO_3$ NSs surface were peculiarly prone to precipitate strontium oxides [40,41], $SrTiO_3$ NSs were treated by NH_4F etching to form Ti−O terminated surface (coded as T-$SrTiO_3$), which is beneficial to the interfacial charge separation. As expected, the resultant 2D/2D T-$SrTiO_3$/$CsPbBr_3$ heterostructure display significantly enhanced activity for CO_2 photoreduction.

The T-$SrTiO_3$/$CsPbBr_3$ composites were prepared by a two-step synthesis method as shown in Fig. S1 (Supporting information), and specific processes were described in Supporting information. Briefly, the $SrTiO_3$ NSs obtained by ethylene glycol assisted solvothermal method [42] were first treated with hot water and NH_4F solution to form Ti−O terminated T-$SrTiO_3$. Then the as-prepared T-$SrTiO_3$ NSs as a substrate were added into the hot-injection reaction system for *in-situ* growth of $CsPbBr_3$ NSs to generate T-$SrTiO_3$/$CsPbBr_3$ composite. For comparison, the $SrTiO_3$/$CsPbBr_3$ composites with untreated $SrTiO_3$ NSs were also synthesized under the same conditions. Transmission electron microscopy (TEM) measurements demonstrated that the as-prepared $SrTiO_3$ samples are layered shape structures with transverse size of about 20−50 nm (Fig. 1a), and the morphology does not change obviously after NH_4F treatment (Fig. 1b). Both the high-resolution TEM (HRTEM) images of $SrTiO_3$ and T-$SrTiO_3$ display 0.19 nm lattice spacing (insets in Figs. 1a and b), corresponding to the (200) crystal plane of $SrTiO_3$. The TEM images of composites (Fig. S2a in Supporting information and Fig. 1c) reveal that the surfaces of $SrTiO_3$ and T-$SrTiO_3$ NSs are successfully decorated with dispersed $CsPbBr_3$ NSs, the sizes of which (~20 nm) are similar to that obtained by identical condition without adding perovskite oxides substrate (Fig. S3 in Supporting information). The corresponding HRTEM images (Fig. S2b in Supporting information and Fig. 1d) exhibit distinct lattice spacing of 0.19 and 0.29 nm, which can be assigned to the (200) lattice planes of cubic phase $SrTiO_3$ and $CsPbBr_3$, respectively. High-angle annular dark-field scanning TEM (HAADF-STEM) and energy-dispersive X-ray spectroscopy (EDS)

mapping measurements (Figs. S4 and S5 in Supporting information) further confirmed the successful generation of $CsPbBr_3$ on the perovskite oxide substrates, showing local concentrated element distributions of Cs, Pb and Br.

We further resorted to Fourier transform infrared (FTIR) spectroscopy to explore the influence of NH_4F etching on the surface structure of $SrTiO_3$. As shown in Fig. 2a, there are distinct characteristic peaks at 2848, 1514, 1371 and 1081 cm⁻¹ for $SrTiO_3$, which can be attributed to the vibrations of C−H, COO⁻, Sr−O and C−C−O, respectively [43]. These characteristic peaks obviously decrease or even disappear in T-$SrTiO_3$, indicating that most of the oxides and incomplete reactants were removed on its surface during the process of treatment. In addition, the stretching vibrations peak of NH_3^+ at 1630 cm⁻¹ [44] in T-$SrTiO_3$ is noticeably increased in comparison with that in $SrTiO_3$, which may be related to the introduction of NH_4F. Meanwhile, the broad absorption peaks at the range of 736 and 559 cm⁻¹ assigned to the Ti−O−Ti stretching vibrations and the TiO_6 octahedron crystal lattice vibrations [45] have obviously enhanced intensity after treatment, indicating the exposure of Ti and O atoms on the surface of the T-$SrTiO_3$ NSs, which provides favorable condition for the tight growth of $CsPbBr_3$. Additionally, the contents of Sr, Ti and O elements on the surface of $SrTiO_3$ before and after treatment have been analyzed by XPS measurements, and the results showed that the content ratio of Sr, Ti and O elements on the surface of initial $SrTiO_3$ is close to 1:1:3, while the corresponding content is 0.55:1:3 after surface treatment (Table S1 in Supporting information). This result provides further strong evidence that Sr was etched during surface treatment.

Furthermore, the powder X-ray diffraction (PXRD) and ultraviolet-visible diffuse reflectance spectroscopy (UV–vis DRS) measurements (Fig. 2b and Fig. S6 in Supporting information) confirmed that the etching of trace NH_4F solution only treated the surface of $SrTiO_3$, while did not change its internal crystal structure and optical absorption. PXRD patterns (Fig. 2b) of the composites have the characteristic diffraction signals of $SrTiO_3$ (JCPDS No. 35−0734) [46] and $CsPbBr_3$ (JCPDS No. 54−0752) [47]. The absorption edges of T-$SrTiO_3$ and $CsPbBr_3$ NSs are 378 and 537 nm, respectively, which can also be clearly observed in T-$SrTiO_3$/$CsPbBr_3$ and $SrTiO_3$/$CsPbBr_3$ composites (Fig. S6). In addition, the X-ray photoelectron spectroscopy (XPS) measurements showed that the binding energy of T-$SrTiO_3$/$CsPbBr_3$ for Sr 3d, Ti 2p and O 1s have perceptible shift to high binding energy
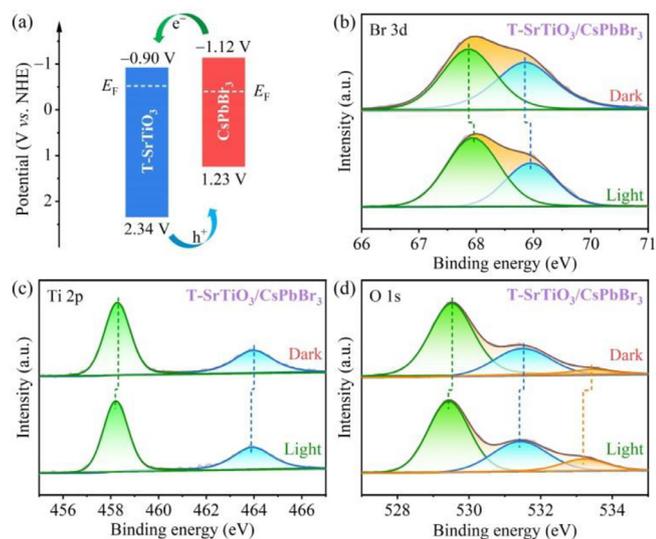
Fig. 3. (a) Energy band diagrams of T-SrTiO$_3$ and CsPbBr$_3$ before contact. High-resolution XPS spectra of (b) Br 3d, (c) Ti 2p and (d) O 1s in T-SrTiO$_3$/CsPbBr$_3$ in the dark and under light irradiation.

Fig. 4. (a) Time-resolved PL decay curves of CsPbBr$_3$, SrTiO$_3$/CsPbBr$_3$ and T-SrTiO$_3$/CsPbBr$_3$. (b) $I-t$ curves and (c) EIS Nyquist plots of SrTiO$_3$, CsPbBr$_3$, SrTiO$_3$/CsPbBr$_3$ and T-SrTiO$_3$/CsPbBr$_3$ under light irradiation. (d) Yields of CO with SrTiO$_3$, CsPbBr$_3$, SrTiO$_3$/CsPbBr$_3$ and T-SrTiO$_3$/CsPbBr$_3$ as photocatalysts, under 300 W Xe lamp with the light intensity of 100 mW/cm^2.

direction compared to those of pristine SrTiO$_3$, while the signals for Cs 3d, Pb 4f and Br 3d move in the opposite direction with respect to individual CsPbBr$_3$ as presented in Figs. 2c, d and S7 (Supporting information). The corresponding binding energies in SrTiO$_3$/CsPbBr$_3$ also have a similar change trend, but the amplitude is obviously weaker, indicating that there are stronger electron coupling between T-SrTiO$_3$ and CsPbBr$_3$ due to the tight contact between T-SrTiO$_3$ and CsPbBr$_3$.

The band gaps (E_g) of T-SrTiO$_3$ and CsPbBr$_3$ were determined by the Tauc plots derived from UV−vis DRS spectra (Fig. S8 in Supporting information), be 3.24 and 2.35 eV, respectively. The valence band edge potentials (E_{VB}) of T-SrTiO$_3$ and CsPbBr$_3$ can be calculated to be 2.34 and 1.23 V relative to normal hydrogen electrode (NHE) by the ultraviolet photoelectron spectroscopy (UPS) measurements (Fig. S9 in Supporting information). Combined with E_g and E_{VB} values, we can derive the conduction band edge potentials (E_{CB}) of T-SrTiO$_3$ and CsPbBr$_3$ to be −0.90 and −1.12 V (*vs.* NHE), respectively. Apparently, the T-SrTiO$_3$/CsPbBr$_3$ heterostructure should show staggered band arrangement as depicted in Fig. 3a. In addition, both T-SrTiO$_3$ and CsPbBr$_3$ feature *n*-type semiconductor characteristics because their Mott−Schottky plots have positive slopes at different frequencies (Fig. S10 in Supporting information). Therefore, their Fermi level (E_F) positions should be biased towards the edges of the corresponding conduction bands, which can be confirmed by the UPS spectra measurements (Fig. S9), locating at −0.52 and −0.41 eV (*vs.* NHE) for T-SrTiO$_3$ and CsPbBr$_3$ (Fig. 3a). When T-SrTiO$_3$ and CsPbBr$_3$ are in close contact, this difference in E_F will drive the transfer of interface free electrons from T-SrTiO$_3$ to CsPbBr$_3$ to achieve the E_F balance of the system. As a result, a built-in electric field pointing from T-SrTiO$_3$ to CsPbBr$_3$ will form at the heterostructure interface.

The resultant built-in electric field and band bending (Fig. S11 in Supporting information) will facilitate the transfer of photogenerated electrons from CsPbBr$_3$ to T-SrTiO$_3$, and *vice versa* for photogenerated holes. The *in-situ* irradiated XPS measurements were further performed to analyze the interfacial charge transfer orientation in T-SrTiO$_3$/CsPbBr$_3$ heterostructure. As shown in Fig. 3b, upon light irradiation, the binding energy of Br 3d in T-SrTiO$_3$/CsPbBr$_3$ shifted positively, which implies that hole accumulation occurred in CsPbBr$_3$. Meanwhile, the binding energies of Ti 2p (Fig. 3c) and O 1s (Fig. 3d) in T-SrTiO$_3$/CsPbBr$_3$ shifted negatively after light irradiation, indicating that the electron density increased around
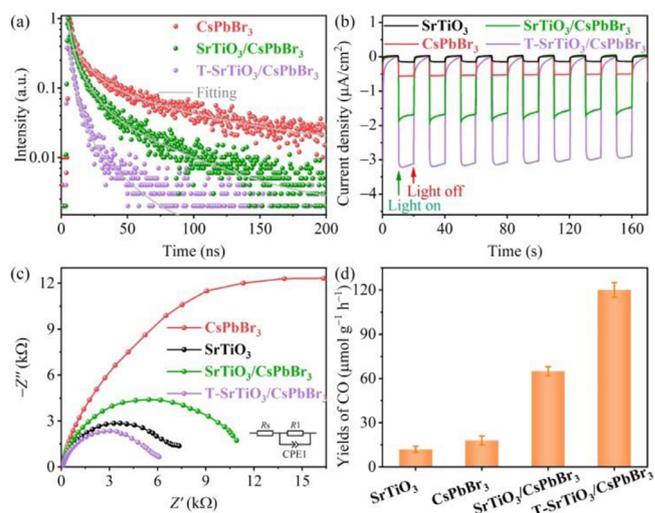
Ti and O cores. These light-induced binding energy shifts confirmed that the photogenerated electrons in CsPbBr$_3$ can transfer to SrTiO$_3$, and the holes in CsPbBr$_3$ can transfer to SrTiO$_3$, which accords with the traditional II type double charge transfer mechanism.

The dynamics of photogenerated carriers in T-SrTiO$_3$/CsPbBr$_3$ heterostructure was further scrutinized by time-resolved photoluminescence (TRPL) measurements. As shown in Fig. 4a, the TRPL decay traces can be well fitted with a three-exponential function to determine the average lifetimes of PL decays (Table S2 in Supporting information). The TRPL decay curve of pure CsPbBr$_3$ NSs denote the radiative and nonradiative processes of photogenerated excitons in CsPbBr$_3$, showing an average lifetime of 43.88 ns. Decorating CsPbBr$_3$ on the surface of SrTiO$_3$ leads to a distinctly accelerated PL decay, and the average PL lifetime is shortened to 23.02 ns, indicating the occurrence of charge transfer between SrTiO$_3$ and CsPbBr$_3$ owing to their favorable energy-offset and the formation built-in electric field (Fig. S11). It is noted that replacing SrTiO$_3$ with T-SrTiO$_3$ results in a further significant acceleration of PL decay with an average PL lifetime of 7.64 ns, which indicates faster charge transfer at the T-SrTiO$_3$/CsPbBr$_3$ heterostructure interface in comparison with that at SrTiO$_3$/CsPbBr$_3$ counterpart, owing to the stronger electron coupling between T-SrTiO$_3$ and CsPbBr$_3$ (Figs. 2c and d). The efficient charge separation in T-SrTiO$_3$/CsPbBr$_3$ can be further proved by photocurrent response ($I-t$) and electrochemical impedance spectroscopy (EIS) experiments. As shown in Fig. 4b, the photocurrent density of T-SrTiO$_3$/CsPbBr$_3$ is significantly higher than those of SrTiO$_3$, CsPbBr$_3$ and SrTiO$_3$/CsPbBr$_3$. T-SrTiO$_3$/CsPbBr$_3$ also shows a smaller diameter of semicircular arc (Fig. 4c) than those of SrTiO$_3$, CsPbBr$_3$ and SrTiO$_3$/CsPbBr$_3$.

A gas-solid reactor (Fig. S12 in Supporting information) was employed to evaluate the photocatalytic CO$_2$ reduction activities of the as-prepared catalysts with water vapor as the electron donor. A 300 W xenon lamp was used as the illuminant with a light intensity of 100 mW/cm^2. The main reduction product was confirmed by gas chromatography analysis to be CO, and there are no other reduction products that could not be ignored (Fig. S13 in Supporting information). The CO formation rates of all photocatalysts were compiled in Fig. 4d. Both the SrTiO$_3$ and CsPbBr$_3$ NSs exhibit very poor photocatalytic activity for CO$_2$ reduction, with the CO

formation rates of 12.1 ± 2.3 and 18.3 ± 3.1 μmol g^{-1} h^{-1}, respectively, owing to the weak light absorption capacity and/or insufficient charge separation efficiency. SrTiO$_3$/CsPbBr$_3$ heterostructure exhibits a significant enhanced activity for CO$_2$ photoreduction, owing to the improved charge separation. Increasing the content of SrTiO$_3$ results in a volcanic tendency for CO$_2$ photoreduction activity (Fig. S14 in Supporting information). The evolution of CO reaches an optimal value of 65.5 ± 3.4 μmol g^{-1} h^{-1} (Fig. 4d), which is about 5.4 and 3.6 times higher than those of individual SrTiO$_3$ and CsPbBr$_3$ nanosheets, respectively. Moreover, the T-SrTiO$_3$/CsPbBr$_3$ heterostructure exhibits a further manifest enhancement of photocatalytic activity for CO$_2$ conversion due to the accelerated interfacial charge transfer. The CO generation rate of T-SrTiO$_3$/CsPbBr$_3$ reaches up to 120.2 ± 4.9 μmol g^{-1} h^{-1}, and the corresponding electron consumption ($R_{electron} = 2n_{CO}$, n_{CO} denote the yield of CO) yield is 240.4 ± 9.8 μmol g^{-1} h^{-1}, which surpasses the reported halide perovskite-based photocatalysts under the same conditions (Table S3 in Supporting information).

In addition, the photocatalytic stability of T-SrTiO$_3$/CsPbBr$_3$ was further estimated by cyclic test. As shown in Fig. S15 (Supporting information), the percentage decrease of CO formation rate after 5 cycles is less than 10%, indicating that T-SrTiO$_3$/CsPbBr$_3$ has good stability in the gas−solid reaction system. Further XRD and XPS measurements confirmed that the structure of T-SrTiO$_3$/CsPbBr$_3$ heterostructure is well maintained after the photocatalytic reaction (Figs. S16 and S17 in Supporting information). Control experiments were further carried out to determine the source of CO using T-SrTiO$_3$/CsPbBr$_3$ as photocatalyst. As shown in Fig. S18 (Supporting information), the product cannot be detected in the absence of light irradiation or photocatalyst, indicating that the CO$_2$ reduction is initiated by light on the photocatalyst. The blank experiment without CO$_2$ showed trace CO, which should be the result of the decomposition of residual surface ligands, indicating that the carbon source of CO mainly comes from CO$_2$. In addition, the control experiment in the absence of water vapor also showed negligible CO production, demonstrating that the electron source of CO$_2$ photoreduction came from water oxidation. These inferences can be further confirmed by $^{13}CO_2$ and $H_2{}^{18}O$ isotope labeling experiments (Fig. S19 in Supporting information). Mass spectrometry (MS) measurements can clearly detect signals at $m/z = 29$ corresponding to ^{13}CO and at $m/z = 36$ assigning to $^{18}O_2$.

To summarize, we have successfully constructed 2D/2D T-SrTiO$_3$/CsPbBr$_3$ heterostructure by lattice-matched *in-situ* growth of CsPbBr$_3$ NSs on surface treated SrTiO$_3$ NSs. Thermodynamic characterization has demonstrated formation of type II heterostructure between T-SrTiO$_3$ and CsPbBr$_3$. The favorable energy-offset and strong electron coupling at heterostructure interface result in an efficient charge separation as confirmed by joint XPS, TRPL and electrochemical investigation, which endows T-SrTiO$_3$/CsPbBr$_3$ heterostructure exhibiting significantly enhanced photocatalytic performance for CO$_2$ reduction, reaching up to an exciting CO yield of 120.2 ± 4.9 μmol g^{-1} h^{-1} in the absence of any organic sacrificial agents, which is about 10 and 7 times higher than that of pure SrTiO$_3$ and CsPbBr$_3$ NSs, respectively. This work provides a simple and versatile strategy for the construction of HP based heterostructures with speedy charge separation to achieve efficient photocatalytic CO$_2$ reduction.

Declaration of competing interest

The authors declare that they have no known competing financial interests or personal relationships that could have appeared to influence the work reported in this paper.

Acknowledgments

Supplementary materials

Supplementary material associated with this article can be found, in the online version, at doi:10.1016/j.cclet.2022.07.025.

References

[1] W. Gao, S. Liang, R. Wang, et al., Chem. Soc. Rev. 49 (2020) 8584–8686.
[2] J. Fu, K. Liu, K. Jiang, et al., Adv. Sci. 6 (2019) 1900796.
[3] J. Fu, K. Jiang, X. Qiu, J. Yu, M. Liu, Mater. Today 32 (2020) 222–243.
[4] K.Q. Lu, Y.H. Li, F. Zhang, et al., Nat. Commun. 11 (2020) 5181.
[5] Y.H. Chen, M.Y. Qi, Y.H. Li, Cell Rep. Phys. Sci. 2 (2021) 100371.
[6] L. Yuan, M.Y. Qi, Z.R. Tang, Y.J. Xu, Angew. Chem. Int. Ed. 60 (2021) 21150–21172.
[7] Q. Wang, J. Warnan, S. Rodríguez-Jiménez, et al., Nat. Energy 5 (2020) 703–710.
[8] W. Zhang, A.R. Mohamed, W.J. Ong, Angew. Chem. Int. Ed. 59 (2020) 22894–22915.
[9] S.N. Habisreutinger, L. Schmidt-Mende, J.K. Stolarczyk, Angew. Chem. Int. Ed. 52 (2013) 7372–7408.
[10] S. Du, J. Lian, F. Zhang, Trans. Tianjin Univ. 28 (2022) 33–52.
[11] J. Wang, S. Lin, N. Tian, et al., Adv. Funct. Mater. 31 (2021) 2008008.
[12] J.D. Xiao, H.L. Jiang, Acc. Chem. Res. 52 (2019) 356–366.
[13] S.F. Ng, M.Y.L. Lau, W.J. Ong, Sol. RRL 5 (2021) 2000535.
[14] C. Dai, B. Liu, Energy Environ. Sci. 13 (2020) 24–52.
[15] J.K. Stolarczyk, S. Bhattacharyya, L. Polavarapu, et al., ACS Catal. 8 (2018) 3602–3635.
[16] J. Fu, S. Wang, Z. Wang, et al., Front. Phys. 15 (2020) 33201.
[17] Y. Wang, T. He, J. Mater. Chem. A 9 (2021) 87–110.
[18] J. Fu, K. Liu, H. Li, et al., Environ. Chem. Lett. 20 (2022) 243–262.
[19] S. Park, W.J. Chang, C.W. Lee, et al., Nat. Energy 2 (2017) 16185.
[20] G. Gao, Q. Xi, H. Zhou, et al., Nanoscale 9 (2017) 12032–12038.
[21] Y.F. Xu, M.Z. Yang, B.X. Chen, et al., J. Am. Chem. Soc. 139 (2017) 5660–5663.
[22] X. Zhu, Y. Lin, Y. Sun, et al., J. Am. Chem. Soc. 141 (2019) 733–738.
[23] M.V. Kovalenko, L. Protesescu, M.I. Bodnarchuk, Science 358 (2017) 745–750.
[24] L.Y. Wu, M.R. Zhang, Y.X. Feng, et al., Sol. RRL 5 (2021) 2100263.
[25] Q. Chen, Y. Ma, L. Wang, et al., Sol. RRL 5 (2021) 2000755.
[26] J. Cheng, Y. Mu, L. Wang, et al., Nano Res. 15 (2022) 1845–1852.
[27] Z. Chen, Y. Hu, J. Wang, et al., Chem. Mater. 32 (2020) 1517–1525.
[28] X. Wang, J. He, J. Li, et al., Appl. Catal. B 277 (2020) 119230.
[29] N.N. Guo, Z.L. Liu, Y.F. Mu, et al., Chin. Chem. Lett. 33 (2022) 3039–3042.
[30] M. Que, Y. Zhao, Y. Yang, et al., ACS Appl. Mater. Interfaces 13 (2021) 6180–6187.
[31] F. Xu, K. Meng, B. Cheng, et al., Nat. Commun. 11 (2020) 4613.
[32] H. Huang, J. Zhao, Y. Du, et al., ACS Nano 14 (2020) 16689–16697.
[33] J. Wang, J. Wang, N. Li, et al., ACS Appl. Mater. Interfaces 12 (2020) 31477–31485.
[34] Y.F. Mu, W. Zhang, G.X. Dong, et al., Small 16 (2020) 2002140.
[35] Y. Jiang, J.F. Liao, H.Y. Chen, et al., Chem 6 (2020) 766–780.
[36] M. Ou, W. Tu, S. Yin, et al., Angew. Chem. Int. Ed. 57 (2018) 13570–13574.
[37] Y. Zhang, Y. Wang, L. Xiong, et al., Chin. Chem. Lett. 33 (2022) 2111–2116.
[38] M.Y. Qi, Q. Lin, Z.R. Tang, Y.J. Xu, Appl. Catal. B 307 (2022) 121158.
[39] J. Chen, D.J. Morrow, Y. Fu, et al., J. Am. Chem. Soc. 139 (2017) 13525–13532.
[40] J.G. Connell, B.J. Isaac, G.B. Ekanayake, et al., Appl. Phys. Lett. 101 (2012) 251607.
[41] M. Kawasaki, K. Takahashi, T. Maeda, et al., Science 266 (1994) 1540–1542.
[42] A. Thesing, E.J. Damiani, L.F. Loguercio, et al., ACS Omega 5 (2020) 33007.
[43] J. Liu, H. Bai, Y. Wang, et al., Adv. Funct. Mater. 20 (2010) 4175–4181.
[44] H.Y. Huang, R.T. Yang, D. Chinn, et al., Ind. Eng. Chem. Res. 42 (2003) 2427–2433.
[45] X. Wu, C. Wang, Y. Wei, et al., J. Catal. 377 (2019) 309–321.
[46] Y. Wei, J. Wang, R. Yu, et al., Angew. Chem. Int. Ed. 58 (2019) 1422–1426.
[47] J. Hou, S. Cao, Y. Wu, et al., Chem. Eur. J. 23 (2017) 9481–9485.